ACS Catalysis

Research Article

Cite This: ACS Catal. 2018, 8, 4508–4515

pubs.acs.org/acscatalysis

Role of Hyper-Reduced States in Hydrogen Evolution Reaction at Sulfur Vacancy in MoS_2

Kye Yeop Kim,[⊥,†,‡] Joohee Lee,[⊥,†] Sungwoo Kang,[†] Young-Woo Son,[§] Ho Won Jang,[†] Youngho Kang,[*,∥] and Seungwu Han[*,†,§]

[†]Department of Materials Science and Engineering and Research Institute of Advanced Materials, Seoul National University, Seoul 08826, Korea

[‡]LG Electronics Yangjae R&D campus, 38, Baumoe-ro, Seocho-gu, Seoul 06763, Korea

[§]Korea Institute for Advanced Study, Seoul 02792, Korea

[∥]Materials Modeling and Characterization Department, Korea Institute of Materials Science, Changwon 51508, Korea

Supporting Information

ABSTRACT: Using the multiscale simulation combining *ab initio* calculations and kinetic Monte Carlo (KMC) simulations, we theoretically investigate the hydrogen evolution reaction (HER) on the sulfur vacancy of a MoS_2 monolayer. Unlike metal catalysts, the protonation step and the charging step proceed independently in semiconducting MoS_2. Interestingly, the barrier for hydrogen evolution decreases when the vacancy site is hyper-reduced with extra electrons. The turnover frequency and polarization curve obtained from the KMC simulation agree well with extant experimental data, and the major HER paths underscore the role of hyper-reduced states, particularly when the overpotential is applied. The strain effect is also simulated, and it is found that the tensile strain enhances HER by reducing the energy cost of hyper-reduced states. The estimated reduction in the overpotential agrees favorably with the experiment while the hydrogen binding energy alone cannot account for it, suggesting that the full-blown KMC simulation should be used to accurately predict the variation of HER performance under various conditions. By uncovering the nature of the catalytic reaction at the sulfur vacancy of MoS_2 and revealing a design principle in which the facile formation of hyper-reduced states plays an important role, the present work will pave the way for developing HER catalysts that may replace Pt.

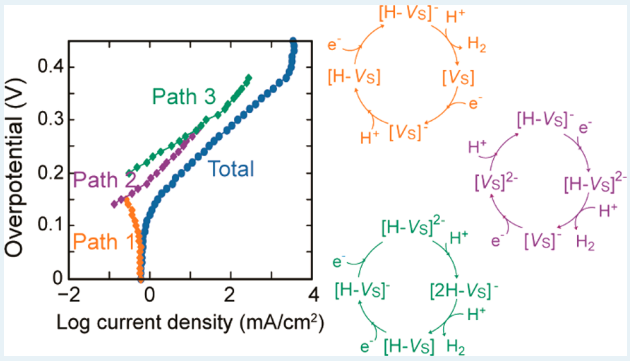

KEYWORDS: *hydrogen evolution reaction, MoS_2, sulfur vacancy, hyper-reduced state, ab initio, kinetic Monte Carlo*

INTRODUCTION

Hydrogen gas (H_2) attracts a great deal of attention as an energy carrier due to high energy density and environmentally benign byproducts at consumption.[1−4] At present, however, hydrogen is mainly generated by burning fossil fuels, which emit CO_2 gas, a cause of global warming. If hydrogen is produced by solar water splitting, CO_2 emission will significantly shrink, thereby achieving sustainable and clean hydrogen production. However, the water splitting through (photo)electrochemical reactions requires an efficient catalyst to lower the overpotential during the hydrogen and oxygen evolution reaction (HER and OER, respectively). Traditionally, noble metals such as platinum have been favored as catalysts for HER owing to their excellent catalytic performances.[5] However, in order to lower the production cost to the level of other competing energy sources, it is necessary to find an alternative HER catalyst.

Recently, transition metal dichalcogenides, particularly molybdenum disulfide (MoS_2), are attracting a great deal of attention as promising HER catalysts.[6−9] MoS_2 has several advantages: it is earth-abundant, is stable in acidic media, and has a two-dimensional nature that may result in a high density of active sites.[7,10] However, the main problem in using MoS_2 as an HER catalyst is that the basal plane of 2H-MoS_2 (simply MoS_2 henceforth) is chemically too stable to play as a catalyst. Therefore, several methods have been suggested to activate MoS_2; in the seminal paper, Hinnemann et al. suggested that the Mo-edge of MoS_2 is active for HER by calculating hydrogen adsorption energy that is a main descriptor of HER activity.[6] This theoretical prediction was confirmed by several experiments.[11−13] It was also found that the metastable 1T-MoS_2 showed high HER activity owing to metallic property and high density of active sites.[14−16]

Recently, Li et al. proposed sulfur vacancy (V_S) on the basal plane of the MoS_2 monolayer as the active site based on the calculated adsorption energy of hydrogen.[17] In addition, the catalytic capability of V_S was predicted to be enhanced by

Received: March 5, 2018
Published: April 12, 2018

DOI: 10.1021/acscatal.8b00883
ACS Catal. 2018, 8, 4508−4515

imposing the tensile strain. The accompanying experiment indeed showed the appreciable HER performance in strained MoS_2 including a large concentration of V_S; the measured overpotential for the MoS_2 film with V_S density of 12.5% and tensile strain of 1.35% was 170 mV at 10 mA/cm^2, that is larger than Pt (59 mV)[17] but smaller than the Mo-edge (310 mV)[14] or 1T-MoS_2 (207 mV).[14] In independent works,[18,19] other groups also confirmed that the basal plane of MoS_2 is activated in the presence of V_S. In particular, these works were able to achieve the low Tafel slopes of 70−80 mV/dec without applying strain. (In ref 18, it was suggested that the low contact resistance is crucial for the small Tafel slope.) Therefore, the defect-induced MoS_2 is a promising avenue to activate two-dimensional dichalcogenides.[20−22]

While the HER performance of V_S of MoS_2 was qualitatively explained on the basis of the hydrogen adsorption energy (ΔG_H),[17] we pay attention to the unique nature of this unconventional catalytic site. That is to say, in contrast to conventional metallic catalysts where electrons or holes are inevitably delocalized on numerous atomic sites, the active site of the V_S-introduced MoS_2 is an atom-sized defect embedded in the semiconductor with the ability to trap charges. As a consequence, the binding of proton (protonation step) and electron transfer (reduction step) can proceed independently at the active site during HER, while they should take place concurrently in the metallic catalysts. Figure 1a displays possible charge states in V_S; in the case of bare sulfur vacancy (V_S), the charge state ranges from −4 to +2 because the a_1 state is fully occupied and doubly degenerate e states are empty. (Details about the structural distortion and changes in the electronic structure induced by V_S are provided in the Supporting Information, which is consistent with refs 17 and 23.) When one hydrogen is bonded to the vacancy site (H-V_S), the charge state ranges from −3 to +1. Similarly, for doubly hydrogenated V_S (2H-V_S), the defect site can be charged from −2 to 0. In order to understand the catalytic behavior in full consideration of such charge variations, a systematic and realistic theoretical study is in demand.

RESULTS AND DISCUSSION

Free Energy and Activation Barrier. We first compute the free energy for every possible state of V_s. Figure 1b shows the schematic of the whole system under pH of zero and potential of U with respect to SHE. The local state of V_S is specified by $[n\text{H-}V_S]^q$ where n $(0 \le n \le 2)$ indicates the number of hydrogen atoms bound to the vacancy and q is the net charge of the defect site with the range depending on n (see Figure 1a). Further hydrogenation, namely $n \ge 3$, is highly unstable such that considering it does not affect our conclusion. With N_{H_2} being the H_2 molecules evolved during HER, the Gibbs free energy in reference to neutral V_S before initiation of HER is formulated as follows (see Supporting Information for a more detailed derivation):

$$G(n, q, N_{H_2}) = G([n\text{H} - V_s]^q) - G([V_s]^0) + q\mu_e^{SHE} - \frac{n}{2}\mu_{H_2} - eU(n + 2N_{H_2} - q) \quad (1)$$

where U is the applied potential and μ_e^{SHE} and μ_{H_2} are the chemical potentials of electrons at the SHE condition, which is equivalent to the reversible hydrogen electrode (RHE) under pH = 0 and H_2 molecules, respectively. In eq 1, μ_e^{SHE} is set to

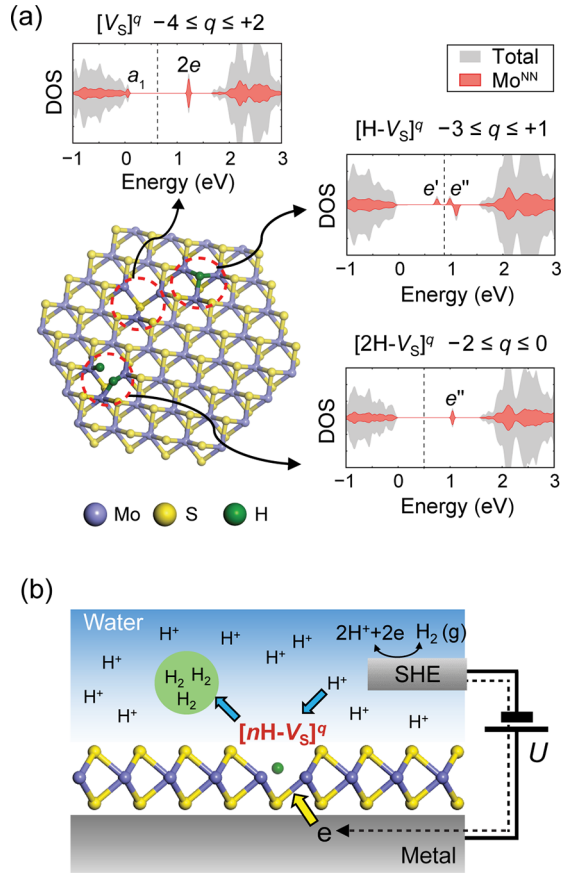

Figure 1. (a) Structure and density of states (DOS) of V_S, H-V_S, and 2H-V_S. The total DOS and partial DOS projected on three nearest-neighbor Mo atoms (Mo^{NN}) around V_S are shown. Possible charge states q for each defect are also noted. The valence band maximum is set to zero and the Fermi levels in the neutral defect state are marked as vertical dashed lines. (b) Schematic illustration of the simulation system including the standard hydrogen electrode (SHE).

−4.44 eV with respect to the vacuum[24,25] and the Gibbs free energies and μ_{H_2} are computed by density-functional theory (DFT) calculations that consider the zero-point energy of hydrogen species, entropic contribution for H_2 gas,[26] and solvation effects.[27] The computational details about DFT calculations and solvation effects are provided in the Methods section.

To calculate the reaction barrier ($\Delta G^{\ddagger}$), possible reaction pathways should be sorted. HER is a stepwise chemical reaction that consists of three elementary steps: Volmer, Heyrovsky, and Tafel steps.[28,29] In the Volmer reaction, a hydronium ion (H_3O^+) in water approaches the active site, leaving one hydrogen ion. The protonation level then changes from V_S to H-V_S or from H-V_S to 2H-V_S. On the other hand, the Heyrovsky step generates hydrogen gas by transferring another hydrogen from H_3O^+, changing H-V_S to H_2+V_S or 2H-V_S to H_2+H-V_S. Lastly, the Tafel step produces H_2 gas from hydrogen atoms bound at the active site, and the state of the active site changes from 2H-V_S to H_2+V_S. We want to note that the charging step, which is assumed to be free of a barrier because the electron transfer is much faster than the protonation step when MoS_2 forms a good contact with the electrode, is separated out from the Volmer and Heyrovsky steps. As a result, $\Delta G^{\ddagger}$ in the following protonation step changes depending on the charge state of catalytic sites.

DOI: 10.1021/acscatal.8b00883
ACS Catal. 2018, 8, 4508−4515

Table 1. Elementary Steps for KMC Simulations and Corresponding ΔG and $\Delta G^{\ddagger}$[a]

Step		Reaction formula	ΔG (eV)	$\Delta G^{\ddagger}$ (eV)
Volmer	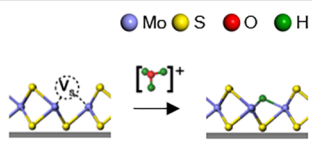	$[V_S] + H^+ \rightarrow [H\text{-}V_S]^+$	0.367	0.513
		$[V_S]^- + H^+ \rightarrow [H\text{-}V_S]^0$	−0.095	0.400
		$[V_S]^{2-} + H^+ \rightarrow [H\text{-}V_S]^-$	−0.566	0.243
		$[V_S]^{3-} + H^+ \rightarrow [H\text{-}V_S]^{2-}$	−0.807	0.000
		$[V_S]^{4-} + H^+ \rightarrow [H\text{-}V_S]^{3-}$	−0.971	0.000
	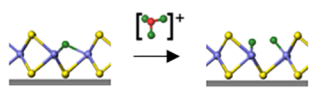	$[H\text{-}V_S]^- + H^+ \rightarrow [2H\text{-}V_S]^0$	0.334	1.018
		$[H\text{-}V_S]^{2-} + H^+ \rightarrow [2H\text{-}V_S]^-$	−0.105	0.660
		$[H\text{-}V_S]^{3-} + H^+ \rightarrow [2H\text{-}V_S]^{2-}$	−0.333	0.395
Heyrovsky	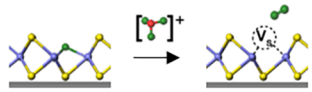	$[H\text{-}V_S]^+ + H^+ \rightarrow [V_S]^{2+} + H_2$	2.208	1.309
		$[H\text{-}V_S]^0 + H^+ \rightarrow [V_S]^+ + H_2$	1.363	1.098
		$[H\text{-}V_S]^- + H^+ \rightarrow [V_S]^0 + H_2$	0.329	0.906
		$[H\text{-}V_S]^{2-} + H^+ \rightarrow [V_S]^- + H_2$	−0.101	0.669
		$[H\text{-}V_S]^{3-} + H^+ \rightarrow [V_S]^{2-} + H_2$	−0.431	0.427
	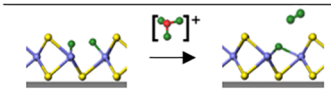	$[2H\text{-}V_S]^0 + H^+ \rightarrow [H\text{-}V_S]^+ + H_2$	0.362	0.906
		$[2H\text{-}V_S]^- + H^+ \rightarrow [H\text{-}V_S]^0 + H_2$	−0.091	0.774
		$[2H\text{-}V_S]^{2-} + H^+ \rightarrow [H\text{-}V_S]^- + H_2$	−0.664	0.644
Tafel	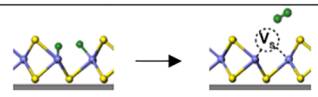	$[2H\text{-}V_S]^0 \rightarrow [V_S]^0 + H_2$	−0.005	1.306
		$[2H\text{-}V_S]^- \rightarrow [V_S]^- + H_2$	0.004	1.294
		$[2H\text{-}V_S]^{2-} \rightarrow [V_S]^{2-} + H_2$	−0.098	1.281
Charging		$[nH\text{-}V_S]^q \rightarrow [nH\text{-}V_S]^{q\pm1}$	Depends on n, q, and U	0

[a]Charging energies are provided in Table S1.

Table 1 compiles all the possible elementary reactions for the subsequent kinetic Monte Carlo (KMC) simulations and corresponding free-energy change (ΔG) and $\Delta G^{\ddagger}$. ΔG values of the reactions are obtained from the difference of free energies calculated by eq 1. To calculate $\Delta G^{\ddagger}$ in Volmer and Heyrovsky steps, we employ the string method[30] combined with the constrained minimization while the nudged-elastic-band (NEB) method[31,32] is employed for the Tafel step. (See the Methods section for more details.) One important tendency in Table 1 is that $\Delta G^{\ddagger}$ decreases monotonically with the magnitude of negative charge at the active site regardless of the hydrogenation level of V_S. Therefore, the vacancy site holding extra electrons—termed the "hyper-reduced state"—can significantly lower the energy barrier for breaking the O−H bond within the hydronium ion, which is the main bottleneck impeding HER. This is because the main contribution to $\Delta G^{\ddagger}$ comes from breaking the O−H bond in H_3O^+ and the negative charge in V_S electrically stabilize H^+ that is being separated from H_3O^+. As will be shown below, the barrier lowering in the charged vacancy plays an important role in accelerating HER.

One may question if the hyper-reduced state is stable in the aqueous solution. The stability of such highly charged states could be tested, albeit indirect, in terms of energy cost to take on charges because high energy states tend to be unstable. For small molecules, the energy cost to take on extra charges is usually high. For example, to add an electron to H_2O or $(H_3O)^+$ requires ∼3 eV in water from our calculations. However, the energy increase is only moderate at the vacancy site of MoS_2 (see Table S1 in the Supporting Information). Specifically, energy costs of charging up to two electrons in V_S, H-V_S, and 2H-V_S are all less than 0.4 eV per an electron. Accordingly, they play dominant roles in HER when the overpotential is applied, as will be discussed below. There are two reasons underlying the low charging energy of V_S in MoS_2: (1) The vacancy states are formed by weak hybridization of d states of neighboring Mo ions that are apart from each other by more than 3 Å. Combined with degeneracy in d manifolds, this leads to a multitude of localized states with similar energies, as can be seen in Figure 1a, which in turn facilitates multiple capturing of electrons at the same vacancy site. This contrasts with molecular systems in which energy levels are significantly split due to strong hybridization among orbitals of constituent elements, and charging of electrons (or holes) incurs a significant energy cost, as illustrated for H_2O or $(H_3O)^+$ in the above. (2) The dielectric screening of surrounding media such as water ($\varepsilon \sim 80$) and MoS_2 ($\varepsilon_{//} \sim 15$)[23] also contributes to stabilizing highly charged states. In particular, the large dielectric constant of water is significantly beneficial. For instance, the free energy change of $[V_S]^{1-} + e^- \rightarrow [V_S]^{2-}$ is 0.99 eV in vacuum, higher than in water by 0.7 eV.

Figure 2a illustrates how $\Delta G^{\ddagger}$ is considered within the KMC simulation (see the Methods section for more details of KMC): the left figure is the Heyrovsky step wherein the protonation on H-V_S generates H_2 gas. The right figure shows a similar procedure, but a charging step (green) precedes the protonation step (orange). The reaction barrier in this case is set to the sum of ΔG for charging and $\Delta G^{\ddagger}$ for protonation. This is a reasonable assumption because the attempt frequency for electron transfer is much higher than that for protonation, and hence the populations of various charge states are equilibrated according to the Boltzmann factor. This effectively lifts the total reaction barrier by ΔG for charging. We also assume that, after each protonation step, the charge state instantly equilibrates to the one with the minimum Gibbs free energy under the same hydrogenation level. Figure 2b illustrates the exemplary event table evolving from $[H\text{-}V_S]$. Each event within the same event table is weighted by reaction

DOI: 10.1021/acscatal.8b00883
ACS Catal. 2018, 8, 4508−4515

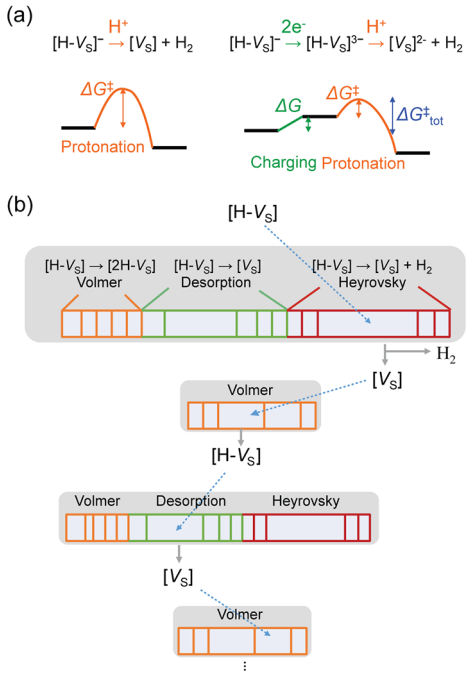

Figure 2. (a) Reaction barrier in KMC simulations. On the left, only protonation is involved while a charging step precedes the protonation on the right. In the latter case, the effective barrier is the sum of charging energy and the protonation barrier. (b) Schematic of KMC evolution. The squares under a specific process denote different charge states, and their widths are proportional to the reaction rate.

rate computed by $\Delta G^{\ddagger}$ and ΔG, and the next event is selected by generating a random number.

Polarization Curve and Major Reaction Paths. Figure 3a shows the number of H_2 molecules evolving over time, obtained by KMC simulations with U of 0, −0.15, and −0.25 V. The linear relationship between time and generated H_2 molecules is confirmed and the turnover frequency (TOF) can be obtained from the slope. The TOFs computed from the slope are 6, 18, and 313 s^{-1} for U = 0, −0.15, and −0.25 V, respectively. The polarization curve and Tafel plots can then be obtained from TOFs at various potentials as displayed in Figures 3b and 3c, respectively. To compare with experiment, we assume the 7% vacancy density in the upper S plane, i.e., one active site per 1.23 nm^2. The reference data extracted from the two experiments[17,19] are displayed in solid lines. Among the data with different vacancy densities, the one with the largest current density is chosen (12.5% in ref 17 and 7% in ref 19). Overall, agreement between theory and experiment is reasonable, in particular considering the fully *ab initio* nature of the simulation and uncertainties in estimating V_S density in experiment. Part of the discrepancy could be attributed to the V_S-V_S interaction at high vacancy densities which may enhance HER.[17]

The Tafel plots in Figure 3c show that the Tafel slope of 75 mV/dec (at 10 mA/cm^2) agrees well with the experimental value of 69 mV/dec in ref 19 in the optimal condition but deviates substantially from 140 mV/dec in ref 17. One possible explanation for this variance would be the voltage drop at the interface between the semiconducting MoS_2 and the metal substrate (see Figure S4a), because insufficient carrier densities in monolayer MoS_2 result in poor electrical coupling such as Schottky contact. Indeed, ref 18 showed that the electrical contact substantially affects the Tafel slope, varying its value

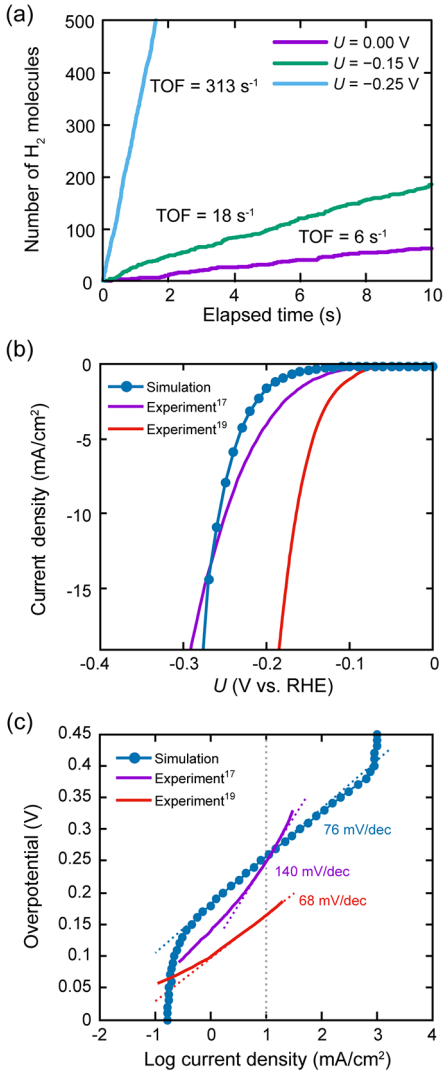

Figure 3. Results of KMC simulations. (a) The number of evolved H_2 molecules as a function of time under a certain potential. Turnover frequencies (TOFs) are obtained by the slope. (b) The computed polarization curve assuming the V_S density of 7% in the upper S plane. For comparison, two experimental curves are adopted from refs 17 and 19 with the V_S densities of 12.5% and 7%, respectively. (c) Tafel plots corresponding to the polarization curves in (b). The Tafel slopes are estimated at 10 mA/cm^2.

from 120 mV/dec (bad contact) to 40−50 mV/dec (good contact). To emulate the contact resistance, we consider the voltage drop by multiplying a scaling factor λ_c ($\leq$1) to U and rerunning the KMC simulations. It is found that the Tafel slope increases monotonically with decreasing λ_c and becomes 127 mV/dec when λ_c is 0.6 (see Figures S4b−c). This might be an overestimation of the contact resistance but demonstrates that the Tafel slope depends significantly on the quality of contact between MoS_2 and the electrode. The chemical interaction and charge transfer between MoS_2 and the support, which are not included in the present study, would also be a potential source of the deviation.[33]

From KMC results, we identify the major reaction paths among hundreds of possible pathways. To this end, we obtain the path-resolved Tafel plots and provide the dominant ones for U = 0, −0.25, and −0.35 V as Path 1, Path 2, and Path 3, respectively, in Figure 4a. All these paths are based on the

DOI: 10.1021/acscatal.8b00883
ACS Catal. 2018, 8, 4508−4515

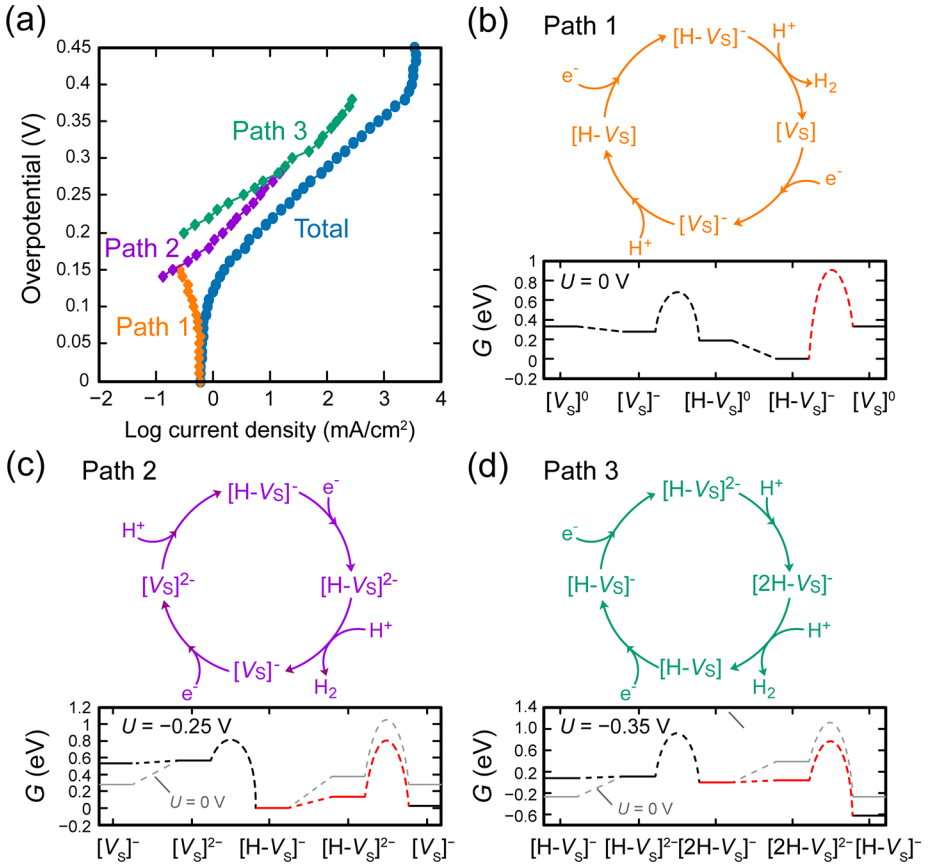

Figure 4. (a) Tafel plot of major paths. Paths 1−3 are the Tafel plots of major paths when overpotential is 0, −0.25, and −0.35 V, respectively. (b−d) The detailed pathways of Path 1−3 in (a). The red line is the rate-limiting step and gray lines in (c) and (d) represent the corresponding path when the potential is 0.

Volmer−Heyrovsky mechanism, and the Volmer−Tafel mechanism has little effect on the hydrogen evolution due to the relatively higher energy barrier in the Tafel step. The same conclusion was also drawn by Voiry et al., who suggested the Volmer−Heyrovsky mechanism as the limiting step based on the experimental Tafel slopes.[18]

The detailed pathways of Paths 1−3 are shown in Figures 4b−d. The rate-limiting step in each path is marked in red. For every U value we examined, the Heyrovsky step turns out to limit the overall reaction rate. Interestingly, Figures 4c and 4d show that the activation barrier of these rate-limiting steps is effectively lowered by going through $[\text{H-}V_S]^{2-}$ or $[\text{2H-}V_S]^{2-}$ prior to the H_2 evolution, when an external potential is applied. This clearly underscores the importance of the hyper-reduced state which reduces the energy barrier for breaking the O−H bond in the hydronium ion. In addition, applying a potential lowers the energy cost for forming the hyper-reduced state, leading to the smaller activation barrier (compare with gray lines corresponding to $U = 0$).

Strain Effect. In experiment, the tensile strain enhanced HER significantly.[17] To investigate the effect of strain, we recalculate the whole set of the ΔG and $\Delta G^{\ddagger}$ at the strain of ±1.35% and obtain the polarization curve as shown in Figure 5a. (See Tables S2 and S3 for ΔG and $\Delta G^{\ddagger}$ under the compressive and tensile strain, respectively.) The current density increases (decreases) when the tensile (compressive) strain is applied. (See Figure S5 for major pathways.) The overpotential with tensile strain decreases by 122 mV compared to the unstrained vacancy, which compares favorably with the experimental decrease of 80 mV.[17]

The influence of strain can be understood in terms of the electronic structure. Figure 5b shows the band structure of monolayer MoS_2 with V_S. When the tensile strain is applied, the occupied a_1 state shifts up while the empty e states shift down compared to the original state. This is due to the bonding and antibonding character of a_1 and e states, respectively. The downshift in energy reduces the energy cost for occupying e states with electrons under the tensile strain, thereby facilitating the formation of hyper-reduced states. For instance, the energy cost for the charging step: $[\text{H} - V_S]^{1-} + e^- \rightarrow [\text{H} - V_S]^{2-}$, the key step at finite overpotentials, is reduced by 0.28 eV under the 1.35% tensile strain. As was seen in Figure 4, the negatively charged states play critical roles in lowering the activation barrier. As such, the tensile strain facilitates the HER reaction. In the case of compressive strain, the opposite happens; that is, the upward shift of the defect levels hinders HER by increasing energy cost to form the hyper-reduced states.

In ref 17, Li et al. accounted for the enhancement of HER activity under the tensile strain in terms of ΔG_H. However, according to the calculations in the reference, the tensile strain of 1.35% reduced ΔG_H by only 0.02 eV. Such a small reduction in ΔG_H cannot explain the substantial decrease of the overpotential by 80 mV at 10 mA/cm^2 in the experiment (this is why the strained and unstrained samples appear to follow different volcano lines in ref 17). This supports that the full-blown KMC simulation is in demand to accurately predict the variations of HER performance under various conditions.

DOI: 10.1021/acscatal.8b00883
ACS Catal. 2018, 8, 4508−4515

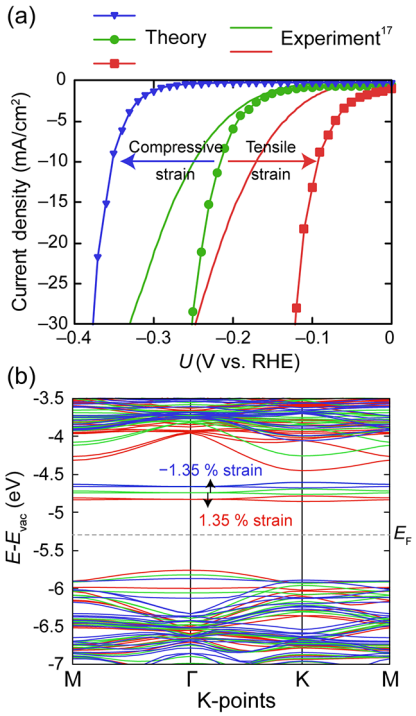

Figure 5. (a) Polarization curves when tensile strain 1.35% and compressive strain −1.35% is applied along with experimental result.[17] (b) The band structure of V_S-MoS_2 when strain is applied. The horizontal dashed line corresponds to the Fermi level in the presence of neutral V_S. The energy is referenced to the vacuum level E_{vac}, and E_F is the Fermi level.

V_S in Various Environments. While the present work focuses on V_S in the monolayer MoS_2, V_S can also be generated in various environments such as edges and multilayer MoS_2, and it would be worthwhile to mention its potential significance in HER. Since the full KMC simulation is costive, we analyze mainly ΔG_H. About V_S in edges, we note that the hyper-reduced state cannot be formed in this case because the metallic character of MoS_2 edges prohibits the charge localization at the vacancy site. We find that the clean edge yields $\Delta G_H \sim 0.12$ eV which is close to the thermoneutral condition, in agreement with the previous work.[6] Interestingly, V_S in the edge also shows a favorable ΔG_H of −0.04 eV, implying that it could serve well as an active site for HER. (The detailed atomic configurations can be found in Figure S6.) Its role, however, is not expected to be as important as vacancy in the basal plane, because the number of active sites is smaller.

The number of MoS_2 layers can be controlled in experiment. To investigate the HER property of V_S in multilayer MoS_2, we evaluate ΔG_H of vacant MoS_2 as a function of the number of MoS_2 underlayers. As expected from the weak interlayer interaction, ΔG_H exhibits very weak dependence of the number of layers (see Table S4), retaining the thermo-neutral condition. Therefore, V_S in multilayer MoS_2 will be also active for HER. However, stacking more MoS_2 layers would impede HER due to the slow electron transfer; Yu et al. demonstrated that the inefficient hopping of a carrier along the vertical direction of multilayer MoS_2 is the biggest concern limiting the overall catalytic performance of multilayer MoS_2.[34]

CONCLUSION

In conclusion, we carried out the full KMC simulation of HER on the vacancy site of MoS_2. To our best knowledge, this is the first attempt to obtain polarization curves using KMC simulations with parameters determined *ab initio*. The protonation and charging steps are assumed to occur independently, due to the semiconducting nature of MoS_2. From the simulation results, it was found that the hyper-reduced states contributed significantly to enhancing HER by lowering the barrier in ensuing protonation. The TOF, polarization curves, and Tafel slope were obtained, which are in good agreement with experiment. The variation of the Tafel slope could be understood in terms of electrical coupling between the metallic substrate and MoS_2. We also identified the major HER paths that depend on the applied potential, which underscores the importance of the hyper-reduced state. The catalytic performance was significantly improved when the tensile strain is applied, because the defect can be easily hyper-reduced owing to downshift of unoccupied defect levels. The change in ΔG_H, the most favored descriptor for HER, turned out to be insufficient to justify the observed strain effect, while the present simulation accounted for the overpotential reduction in experiment. In conclusion, by investigating the unconventional catalytic reaction at the defective MoS_2, we revealed a new design principle that the facile formation of hyper-reduced states in semiconductors enhances HER. As such the present work will pave the way for developing a new class of HER catalysts. In addition, the present theoretical framework is general and so it can also be applied to more complicated processes such as OER.

METHODS

Density Functional Calculation. We performed *ab initio* calculations based on DFT using the Vienna *ab initio* Simulation Package (VASP).[35] The electron−ion interaction was described by the projected-augmented-wave pseudopotential.[36] For the exchange-correlation energies between electrons, the Perdew−Burke−Ernzerhof (PBE) functional was employed.[37] The energy cutoff for the plane-wave basis expansion was chosen to be 350 eV. We sampled a 2 × 2 × 1 *k*-point grid for the integration of the Brillouin zone. This set of computational parameters ensures the convergence of the total energy and atomic forces within 10 meV/atom and 0.02 eV/Å, respectively. The ionic positions were relaxed until atomic forces on each atom were below 0.02 eV/Å. We used 6 × 6 supercells to compute ΔG's of elementary reactions. (ΔG changes negligibly by increasing the supercell size from 3 × 3 to 6 × 6.) Since the calculation of $\Delta G^{\ddagger}$ requires a high computational cost, 3 × 3 supercells were employed for obtaining the energy barrier. A vacuum region with 15 Å thickness was added and electrostatic dipole interactions between repeated slabs were eliminated. To account for effects of water, we included the solvation effect using the implicit solvation model that approximates solvent molecules with a continuum dielectric.[27] The parameters used in the solvation model are 80.0 (dielectric constant), 0.0025 $Å^{-3}$ (cutoff density), 0.6 Å (cavity width), and 0.525 meV/$Å^2$ (surface tension). For a test, we calculated solvation energies of a water molecule and hydronium ion, obtaining −0.31 and −4.65 eV that are in good agreement with experimental values (−0.27 and −4.78 eV, respectively).[38] In a charged system, the total energy is affected by the spurious interaction between repeated

DOI: 10.1021/acscatal.8b00883
ACS Catal. 2018, 8, 4508−4515

images within periodic boundary condition, which should be corrected to obtain the free energy in a dilute limit. In the present study, the energy required for the correction was found to be negligible due to the high dielectric constant of water.

Calculation of Kinetic Barriers of Protonation Steps. For protonation steps, hydronium ions (H_3O^+) are considered as a stable state of proton in water. We found that the solvation model is important to maintain the charge state of H_3O^+ when the MoS_2 slab coexists in the computational cell. (See Figure S2). Since the NEB method in conjunction with solvation effects converges very slowly, we obtained the potential energy surface by the constrained minimization and found the minimum energy path using the string method.[30] (See Figure S3 for the example of a Volmer step.)

Kinetic Monte Carlo Simulation. In the KMC simulations, all the possible elementary steps are taken into account. If the free energy difference between the reactant and product is ΔG and the activation energy in the forward direction is $\Delta G^{\ddagger}$, forward and backward reaction rates are as follows:

$$r_{\text{forward}} = \Gamma \exp\left(-\frac{\Delta G^{\ddagger}}{k_B T}\right) \tag{2}$$

$$r_{\text{backward}} = \Gamma \exp\left(-\frac{\Delta G + \Delta G^{\ddagger}}{k_B T}\right) \tag{3}$$

We adopt $k_B T/h$ as prefactor Γ, which is a favored choice in estimating the rate constant of the dissociation of a hydrogen molecule.[39] To consider tunneling effects of hydrogen in the protonation step, the barrier is scaled down by 0.75, which is obtained by fitting the effective barrier to the Wentzel–Kramers–Brillouin (WKB) results.[40]

■ ASSOCIATED CONTENT

Supporting Information

The Supporting Information is available free of charge on the ACS Publications website at DOI: 10.1021/acscatal.8b00883.

Detailed electronic and structural character of V_S, details of free energy calculation, tables for charging energies of active site, solvation effects on the transition state, details of string method, concept and influence of contact resistance, Gibbs free energies of various states of active site with strain, major paths on different conditions of strain, hydrogen binding energy of V_S in Mo-edge and multilayer MoS_2 (PDF)

■ AUTHOR INFORMATION

Corresponding Authors

*E-mail: thehoya84@gmail.com.
*E-mail: hansw@snu.ac.kr.

ORCID

Ho Won Jang: 0000-0002-6952-7359
Youngho Kang: 0000-0003-4532-0027

Author Contributions

⊥K.Y.K. and J.L. contributed equally to this work.

Notes

The authors declare no competing financial interest.

■ ACKNOWLEDGMENTS

We thank Hyungjun Kim for helpful discussions. This work was supported by the Samsung Research Funding Center of Samsung Electronics. The computations were performed at the KISTI supercomputing center (Grant No. KSC-2017-C3-0019). Youngho Kang acknowledges the Fundamental Research Program (PNK5260) of the Korea Institute of Materials Science, Republic of Korea.

■ REFERENCES

(1) Dresselhaus, M. S.; Thomas, I. Alternative energy technologies. *Nature* **2001**, *414*, 332–337.
(2) Turner, J. A. Sustainable hydrogen production. *Science* **2004**, *305*, 972–974.
(3) Lewis, N. S.; Nocera, D. G. Powering the planet: chemical challenges in solar energy utilization. *Proc. Natl. Acad. Sci. U. S. A.* **2006**, *103*, 15729–15735.
(4) Abbasi, T.; Abbasi, S. A. 'Renewable'hydrogen: prospects and challenges. *Renewable Sustainable Energy Rev.* **2011**, *15*, 3034–3040.
(5) Trasatti, S. Work function, electronegativity, and electrochemical behavior of metals: III. Electrolytic hydrogen evolution in acid solutions. *J. Electroanal. Chem. Interfacial Electrochem.* **1972**, *39*, 163–184.
(6) Hinnemann, B.; Moses, P. G.; Bonde, J.; Jørgensen, K. P.; Nielsen, J. H.; Horch, S.; Chorkendorff, I.; Nørskov, J. K. Biomimetic hydrogen evolution: MoS_2 nanoparticles as catalyst for hydrogen evolution. *J. Am. Chem. Soc.* **2005**, *127*, 5308–5309.
(7) Merki, D.; Hu, X. Recent developments of molybdenum and tungsten sulfides as hydrogen evolution catalysts. *Energy Environ. Sci.* **2011**, *4*, 3878–3888.
(8) Benck, J. D.; Hellstern, T. R.; Kibsgaard, J.; Chakthranont, P.; Jaramillo, T. F. Catalyzing the hydrogen evolution reaction (HER) with molybdenum sulfide nanomaterials. *ACS Catal.* **2014**, *4*, 3957–3971.
(9) Vesborg, P. C. K.; Seger, B.; Chorkendorff, I. Recent development in hydrogen evolution reaction catalysts and their practical implementation. *J. Phys. Chem. Lett.* **2015**, *6*, 951–957.
(10) Laursen, A. B.; Kegnæs, S.; Dahl, S.; Chorkendorff, I. Molybdenum sulfides-efficient and viable materials for electro-and photocectrocatalytic hydrogen evolution. *Energy Environ. Sci.* **2012**, *5*, 5577–5591.
(11) Jaramillo, T. F.; Jørgensen, K. P.; Bonde, J.; Nielsen, J. H.; Horch, S.; Chorkendorff, I. Identification of active edge sites for electrochemical H_2 evolution from MoS_2 nanocatalysts. *Science* **2007**, *317*, 100–102.
(12) Kong, D.; Wang, H.; Cha, J. J.; Pasta, M.; Koski, K. J.; Yao, J.; Cui, Y. Synthesis of MoS_2 and $MoSe_2$ films with vertically aligned layers. *Nano Lett.* **2013**, *13*, 1341–1347.
(13) Xie, J.; Zhang, H.; Li, S.; Wang, R.; Sun, X.; Zhou, M.; Zhou, J.; Lou, X. W.; Xie, Y. Defect-rich MoS_2 ultrathin nanosheets with additional active edge sites for enhanced electrocatalytic hydrogen evolution. *Adv. Mater.* **2013**, *25*, 5807–5813.
(14) Voiry, D.; Salehi, M.; Silva, R.; Fujita, T.; Chen, M.; Asefa, T.; Shenoy, V. B.; Eda, G.; Chhowalla, M. Conducting MoS_2 nanosheets as catalysts for hydrogen evolution reaction. *Nano Lett.* **2013**, *13*, 6222–6227.
(15) Lukowski, M. A.; Daniel, A. S.; Meng, F.; Forticaux, A.; Li, L.; Jin, S. J. Enhanced hydrogen evolution catalysis from chemically exfoliated metallic MoS_2 nanosheets. *J. Am. Chem. Soc.* **2013**, *135*, 10274–10277.
(16) Chou, S. S.; Sai, N.; Lu, P.; Coker, E. N.; Liu, S.; Artyushkova, K.; Luk, T. S.; Kaehr, B.; Brinker, C. J. Understanding catalysis in a multiphasic two-dimensional transition metal chalcogenide. *Nat. Commun.* **2015**, *6*, 8311.
(17) Li, H.; Tsai, C.; Koh, A. L.; Cai, L.; Contryman, A. W.; Fragapane, A. H.; Zhao, J.; Han, H. S.; Manoharan, H. C.; Abild-Pedersen, F.; Nørskov, J. K.; Zheng, X. Activating and optimizing MoS_2 basal planes for hydrogen evolution through the formation of strained sulphur vacancies. *Nat. Mater.* **2016**, *15*, 48–53.
(18) Voiry, D.; Fullon, R.; Yang, J.; Silva, C.; Kappera, R.; Bozkurt, I.; Kaplan, D.; Lagos, M. J.; Batson, P. E.; Gupta, G.; Mohite, A. D.;

DOI: 10.1021/acscatal.8b00883
ACS Catal. 2018, 8, 4508–4515

Dong, L.; Er, D.; Shenoy, V. B.; Asefa, T.; Chhowalla, M. The role of electronic coupling between substrate and 2D MoS_2 nanosheets in electrocatalytic production of hydrogen. *Nat. Mater.* **2016**, *15*, 1003−1009.
(19) Li, G.; Zhang, D.; Qiao, Q.; Yu, Y.; Peterson, D.; Zafar, A.; Kumar, R.; Curtarolo, S.; Hunte, F.; Shannon, S.; Zhu, Y.; Yanfg, W.; Cao, L. All the catalytic active sites of MoS_2 for hydrogen evolution. *J. Am. Chem. Soc.* **2016**, *138*, 16632−16638.
(20) Lin, L.; Mioa, N.; Wen, Y.; Zhang, S.; Ghosez, P.; Sun, Z.; Allwood, D. A. Sulfur-depleted monolayered molybdenum disulfide nanoctrystals for superelectrochemical hydrogen evolution reaction. *ACS Nano* **2016**, *10*, 8929−8937.
(21) Xu, Y.; Wang, L.; Liu, X.; Zhang, S.; Liu, C.; Yan, D.; Zeng, Y.; Pei, Y.; Liu, Y.; Luo, S. Monolayer MoS_2 with S vacancies from interlayer spacing expanded counterparts for highly efficient electrochemical hydrogen production. *J. Mater. Chem. A* **2016**, *4*, 16524−16530.
(22) Lu, A. Y.; Yang, X.; Tseng, C. C.; Min, S.; Lin, S. H.; Hsu, C. L.; Li, H.; Idriss, H.; Kuo, J. L.; Huang, K. W.; Li, L. J. High-sulfur-vacancy amorphous molybdenum sulfide as a high current electrocatalyst in hydrogen evolution. *Small* **2016**, *12*, 5530−5537.
(23) Noh, J. Y.; Kim, H.; Kim, Y. S. Stability and electronic structures of native defect in single-layer MoS_2. *Phys. Rev. B: Condens. Matter Mater. Phys.* **2014**, *89*, 205417.
(24) Trasatti, S. The absolute electrode potential: an explanatory note (Recommendations 1986). *Pure Appl. Chem.* **1986**, *58*, 955−956.
(25) Trasatti, S. Surface science and electrochemisty: concepts and problems. *Surf. Sci.* **1995**, *335*, 1−9.
(26) Lide, D. R.; Data, S. R.; Board, E. A.; Baysinger, G.; Chemistry, S.; Library, C. E.; Berger, L. I.; Goldberg, R. N.; Division, B.; Kehiaian, H. V; Kuchitsu, K.; Rosenblatt, G.; Roth, D. L.; Zwillinger, D. *CRC Handbook of Chemistry and Physics*; CRC Press: Boca Raton, 2014.
(27) Mathew, K.; Sundararaman, R.; Letchworth-Weaver, K.; Arias, T. A.; Hennig, R. G. J. Implicit solvation model for density-functional study of nanocrystal surfaces and reaction pathways. *J. Chem. Phys.* **2014**, *140*, 084106.
(28) de Chialvo, M. R. G.; Chialvo, A. C. J. Hydrogen evolution reaction − analysis of the Volmer-Heyrovsky-Tafel mechanism with a generalized adsorption model. *J. Electroanal. Chem.* **1994**, *372*, 209−223.
(29) Kibler, L. A. Hydrogen electrocatalysis. *ChemPhysChem* **2006**, *7*, 985−991.
(30) E, W.; Ren, W.; Vanden-Eijnden, E. String method for the study of rare events. *Phys. Rev. B: Condens. Matter Mater. Phys.* **2002**, *66*, 052301.
(31) Mills, G.; Jónsson, H.; Schenter, G. K. Reversible work transition state theory: application to dissociative adsorption of hydrogen. *Surf. Sci.* **1995**, *324*, 305−337.
(32) Henkelman, G.; Uberuaga, B. P.; Jónsson, H. J. A climbing image nudged elastic band method for finding saddle points and minimum energy paths. *J. Chem. Phys.* **2000**, *113*, 9901−9904.
(33) Tsai, C.; Chan, K.; Nørskov, J. K.; Abild-Pedersen, F. Rational design of MoS_2 catalysts: tuning the structure and activity *via* transition metal doping. *Catal. Sci. Technol.* **2015**, *5*, 246−253.
(34) Yu, Y.; Huang, S.-Y.; Li, Y.; Steinmann, S. N.; Yang, W.; Cao, L. Layer-dependent electrocatalysis of MoS_2 for hydrogen evolution. *Nano Lett.* **2014**, *14*, 553−558.
(35) Kresse, G.; Furthmüller, J. Efficient iterative schemes for *ab initio* total-energy calculations using a plane-wave basis set. *Phys. Rev. B: Condens. Matter Mater. Phys.* **1996**, *54*, 11169.
(36) Blöchl, P. E. Projector augmented-wave method. *Phys. Rev. B: Condens. Matter Mater. Phys.* **1994**, *50*, 17953.
(37) Perdew, J. P.; Burke, K.; Ernzerhof, M. Generalized gradient approximation made simple. *Phys. Rev. Lett.* **1996**, *77*, 3865.
(38) Palascak, M. W.; Shields, G. C. J. Accurate experimental values for the free energies of hydration of H^+, OH^-, and H_3O^+. *J. Phys. Chem. A* **2004**, *108*, 3692−3694.
(39) Huang, L.; Nielsen, R. J.; Goddard, W. A.; Soriaga, M. P. The reaction mechanism with free energy barriers for electrochemical dihydrogen evolution on MoS_2. *J. Am. Chem. Soc.* **2015**, *137*, 6692−6698.
(40) Lill, M. A.; Helms, V. J. Reaction rates for proton transfer over small barriers and connection to transition state theory. *J. Chem. Phys.* **2001**, *115*, 7985−7992.

DOI: 10.1021/acscatal.8b00883
ACS Catal. 2018, 8, 4508−4515